Eur. Phys. J. E manuscript No.
(will be inserted by the editor)

Pseudo-turbulence in two-dimensional buoyancy driven bubbly flows: a DNS study

Rashmi Ramadugu,Vikash Pandey, and Prasad Perlekar

TIFR Center for Interdisciplinary Sciences, Hyderabad, 500107, India
e-mail: rashmir@tifrh.res.in

March 17, 2022

Abstract. We present a direct numerical simulation (DNS) study of buoyancy driven bubbly flows in two-dimensions. We employ volume of fluid (VOF) method to track the bubble interface. To investigate spectral properties of the flow, we derive the scale-by-scale energy budget equation. We show that the Galilei number (Ga) controls different scaling regimes in the energy spectrum. For high Galilei numbers, we find the presence of an inverse energy cascade. Our study indicates that the density ratio of the bubble with the ambient fluid or the presence of coalescence between the bubbles does not alter the scaling behaviour.

PACS. 47.55.D- Drops and bubbles

1 Introduction

A swarm of bubbles rising under gravity generates complex spatio-temporal flow patterns, often referred to as pseudo-turbulence (PT) or bubble induced agitation. Although the trajectory and wake of an isolated bubble depend on its viscosity and density contrast with the surrounding fluid [1–6], the statistical properties of the flow generated by the bubble swarm are found to be universal [7–11]. A key feature of PT is the power-law scaling in the energy spectrum with an exponent of -3 either in frequency f or the wave-number k space [8,12–14], explained by the balance of energy production by wakes with viscous dissipation [9,11,15].

The key non-dimensional numbers that characterise pseudo-turbulence are the Bond number $\mathrm{Bo} \equiv \delta\rho g d^2/\sigma$ (ratio of the buoyancy forces to the surface tension forces), the Galilei number $\mathrm{Ga} \equiv \sqrt{\rho_f \delta\rho g d^3}/\mu$ (ratio of the buoyancy forces to the viscous forces), and the Atwood number $\mathrm{At} \equiv \delta\rho/(\rho_f + \rho_b)$, where ρ_f is the density of the ambient fluid, ρ_b is the bubble density, $\delta\rho \equiv \rho_f - \rho_b$, g is the acceleration due to gravity, and d is the initial bubble diameter.

Experiments in three-dimensions (3D) at low volume fraction $\phi \approx 2\%$ observe the k^{-3} scaling in the energy spectrum both within and in the wake of the bubble swarm for $202 \leq \mathrm{Ga} \leq 396$ [12]. In Hele-Shaw geometry, experiments [14,16] at moderate volume fraction $\phi \approx 5 - 16\%$ and $650 \leq \mathrm{Ga} \leq 1100$ also observe the k^{-3} scaling.

Most numerical studies have investigated PT in 3D [11,17,18] and found that the statistical properties of the flow to be universal for a wide range of Atwood At, Bond Bo, and Galilei Ga numbers. Using a scale-by-scale energy budget analysis, Ref. [11] showed that both the surface tension and kinetic energy flux contribute to the net energy production at scales smaller than d.

In comparison to 3D, there have been very few studies on two-dimensional (2D) bubbly flows. Early numerical simulations at low $\mathrm{Ga} = 5.4$ [19] indicated the presence of a k^{-3} scaling regime. Recent high-resolution direct numerical simulation (DNS) in 2D at high Ga show the presence of a k^{-3} scaling for scales smaller than the bubble diameter and an inverse energy cascade for larger scales both within [20] and in the wake of a swarm [21].

Turbulence in two-dimensions is fundamentally different from its counterpart in three-dimensions; in the inviscid limit ($\nu \to 0$), conservation of kinetic energy leads to an inverse energy cascade from forcing scales to large-scales and a direct enstrophy cascade from forcing scales to small scales [22–30]. On the other hand, only a forward energy cascade is possible in three-dimensions because of finite energy dissipation even when viscosity tends to zero [27,31,32].
Several numerical and experimental studies of homogeneous, isotropic turbulence in two- and three-dimensions have studied and verified the proposed energy transfer mechanisms and scaling laws in real and spectral space [27,29–34]. Scale-by-scale energy budget analysis provides a natural way to investigate the interaction between different length scales.
In this paper, we present a DNS study in 2D to investigate pseudo-turbulence generated by buoyancy-driven bubbly flows for small and large Ga, At, and Bo numbers. We characterize the flow in terms of the bubble size distribution, energy spectrum, and use the scale-by-scale energy

budget analysis to study energy transfer mechanisms. Below we summarize the main results of our DNS study:

1. The average bubble diameter $D \sim \mathrm{Bo}^{-1/2}$ in a bubbly flow.
2. The PT k^{-3} scaling in the energy spectrum appears for scales larger than the bubble diameter for small Ga, whereas it appears for scales smaller than the bubble diameter for large Ga.
3. For large Ga, we observe the presence of an inverse energy cascade and a $k^{-5/3}$ scaling in the energy spectrum for scales larger than the bubble diameter.
4. Our scale-by-scale energy budget analysis for large Ga reveals: (i) a negative energy flux for scales larger than the bubble diameter, and (ii) the net energy production balances viscous dissipation for scales smaller than the bubble diameter.

The rest of this paper is organised as follows. In Section. 2, we present the governing equations and the details of our DNS. In Section 3, we discuss our results on buoyancy driven bubbly flows. We present our conclusions in Section 4.

2 Model and Numerical Details

We study the dynamics of bubbly flow by using Navier-Stokes (NS) equations with a surface tension force because of bubbles

$$D_t c = 0, \text{ and } \nabla \cdot \boldsymbol{u} = 0, \tag{1a}$$
$$\rho(c) D_t \boldsymbol{u} = \nabla \cdot [2\mu(c)\mathcal{S}] - \nabla p + \boldsymbol{F}^{\sigma} + \boldsymbol{F}^{g}. \tag{1b}$$

Here, $D_t = \partial_t + (\boldsymbol{u} \cdot \nabla)$ is the material derivative, c is an indicator function whose value is 0 inside the bubble phase and 1 in the fluid phase. $\boldsymbol{F}^{\sigma} \equiv \sigma\kappa\nabla c$ is the force because of the surface tension [37,38], $\boldsymbol{F}^{g} \equiv [\rho_a - \rho(c)]g\hat{\boldsymbol{e}}_y$ is the buoyancy force, $\boldsymbol{u} = (u_x, u_y)$ is the hydrodynamic velocity, p is the pressure, the local density $\rho(c) \equiv \rho_f c + \rho_b(1-c)$, the local viscosity $\mu(c) \equiv \mu_f c + \mu_b(1-c)$, ρ_b (ρ_f) is the bubble (fluid) density, μ_b (μ_f) is the bubble (fluid) viscosity, $\phi \equiv [\int (1-c) d\boldsymbol{x}]/L^2$ is the bubble volume fraction, $\mathcal{S} \equiv (\nabla \boldsymbol{u} + \nabla \boldsymbol{u}^T)/2$ is the rate of deformation tensor, σ is the coefficient of surface tension and κ is the curvature. For small Atwood numbers, Eq. (1b) can be further simplified by invoking Boussinesq approximation whereby, $\rho(c)$ in the left-hand-side of Eq. (1b) is replaced by the average density $\rho_a = \overline{\rho(c)} \approx (\rho_f + \rho_b)/2$, where the $\overline{(.)}$ denotes spatial averaging.

We use a periodic box of volume L^2 and discretize it with N^2 collocation points. We initialize the simulation with a quiescent flow-field $\boldsymbol{u}(\boldsymbol{x}, t=0) = 0$ and place N_b bubbles at random positions well-separated from each other. We numerically integrate Eq. (1) using a second-order accurate volume of fluid (VOF) solver Basilisk [38, 39] which has been used to study a variety of multiphase flow problems. For a review of various numerical schemes used for multiphase flows and comparison between them, we refer the reader to Refs. [39–41]. The parameters that we use in our DNS are listed in Table 1.

3 Results

In Fig. (1) we plot kinetic energy $E \equiv \overline{\rho u^2/2}$ versus t/τ_s for our runs `NB2` $-$ `NB4` (Ga $= 5.4$, At $= 0.9$), `NB6` $-$ `NB8` (Ga $= 312$, At $= 0.08$), and `NB10` $-$ `NB12` (Ga $= 723$, At $= 0.75$), where $\tau_s = L/\sqrt{gd}$ is the approximate time taken by an isolated bubble to traverse the entire domain. After an initial transient, a statistically steady state is attained where the bubbles continuously merge and break to form a stationary suspension.

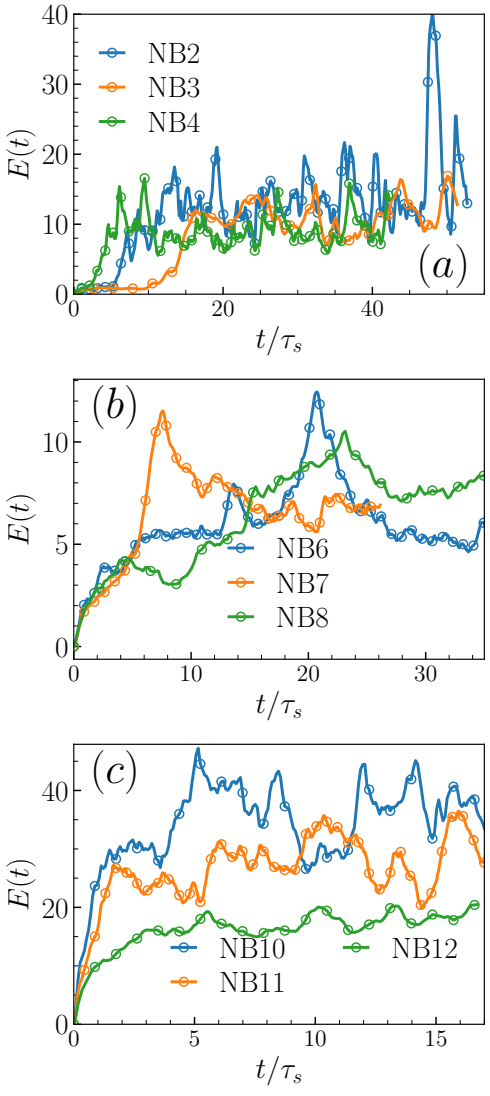

Fig. 1. Plot of kinetic energy ($E(t)$) versus time for (a) runs `NB2-NB4` (Ga $= 5.4$, At $= 0.9$), (b) runs `NB6-NB8` (Ga $= 312$, At $= 0.08$), and (c) runs `NB10-NB12` (Ga $= 723$, At $= 0.75$).

Table 1. The parameters N,L, d, Ga, N_b, Bo, ϕ, At, the viscous dissipation ϵ_μ, and the energy injected due to buoyancy ϵ_{inj} for non-Boussinesq (`NB`) and Boussinesq (`B`) runs. We use front-tracking method [35] for the Boussinesq runs where coalescence is arrested. N_b represent initial number of bubbles. We choose $\mu_f/\mu_b = 1$ and $g = 1$ for all the runs except `NB1 - NB5` where $\mu_f/\mu_b = 20$. All the simulations were conducted at TIFR-H Kohinoor3 cluster [36]. The high Ga runs took ≈ 5 hours for $1\tau_s$ on 64 CPUs.

runs	L	d	N	ρ_f	Ga	N_b	Bo	ϕ	At	ϵ_μ	ϵ_{inj}	ϵ_w
`NB1`	12^2	0.4	1024^2	25.0	2.7	144	1.0	0.12	0.9	2.1 ± 0.6	1.8 ± 0.1	1.5
`NB2`	12^2	0.4	1024^2	25.0	5.4	144	0.5	0.12	0.9	1.3 ± 0.7	0.9 ± 0.1	1.6
`NB3`	12^2	0.4	1024^2	25.0	5.4	144	1.0	0.12	0.9	1.9 ± 0.1	1.8 ± 0.1	1.5
`NB4`	12^2	0.4	1024^2	25.0	5.4	144	2.0	0.12	0.9	0.9 ± 0.1	1.3 ± 0.2	1.2
`NB5`	12^2	0.4	1024^2	25.0	16	144	1.0	0.12	0.9	1.2 ± 0.1	1.4 ± 0.1	1.5
`NB6`	512^2	20.0	2048^2	1.12	312	144	0.5	0.17	0.08	$(2.8 \pm 0.7) \cdot 10^{-2}$	$(3.4 \pm 0.2) \cdot 10^{-2}$	$3.9 \cdot 10^{-2}$
`NB7`	512^2	20.0	2048^2	1.12	312	144	1.0	0.17	0.08	$(2.8 \pm 0.3) \cdot 10^{-2}$	$(3.1 \pm 0.6) \cdot 10^{-2}$	$3.3 \cdot 10^{-2}$
`NB8`	512^2	20.0	2048^2	1.12	312	144	5.0	0.17	0.08	$(1.8 \pm 0.2) \cdot 10^{-2}$	$(2.0 \pm 0.1) \cdot 10^{-2}$	$2.2 \cdot 10^{-2}$
`NB9`	512^2	25.0	2048^2	1.08	312	100	1.0	0.19	0.08	$(3.2 \pm 0.1) \cdot 10^{-2}$	$(3.2 \pm 0.2) \cdot 10^{-2}$	$4.0 \cdot 10^{-2}$
`NB10`	512^2	20.0	2048^2	1.12	723	144	0.5	0.17	0.75	$(3.3 \pm 0.2) \cdot 10^{-1}$	$(4.6 \pm 0.5) \cdot 10^{-1}$	$5.2 \cdot 10^{-1}$
`NB11`	512^2	20.0	2048^2	1.12	723	144	1.0	0.17	0.75	$(3.0 \pm 0.1) \cdot 10^{-1}$	$(3.9 \pm 0.5) \cdot 10^{-1}$	$4.6 \cdot 10^{-1}$
`NB12`	512^2	20.0	2048^2	1.12	723	144	10.0	0.17	0.75	$(2.7 \pm 0.8) \cdot 10^{-1}$	$(3.4 \pm 0.6) \cdot 10^{-1}$	$2.5 \cdot 10^{-1}$
`B1`	512^2	25.0	4096^2	1.0	312	100	0.5	0.19	0.08	$(3.5 \pm 0.3) \cdot 10^{-2}$	$(3.3 \pm 0.3) \cdot 10^{-2}$	$3.0 \cdot 10^{-2}$

In Fig. (2) we show the representative plots of the steady-state velocity streamlines overlaid with bubble positions for Ga = 5.4 and Ga = 723. For low Ga numbers, the typical flow eddies are larger or comparable to the bubbles in the suspension [19], whereas at high Ga numbers smaller eddies are also formed.

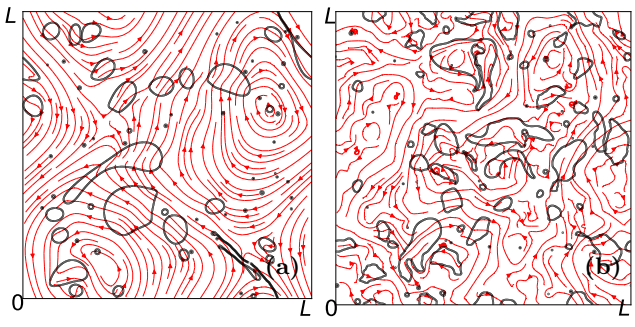

Fig. 2. Instantaneous velocity streamline in the steady-state with overlaid bubble positions for our runs `NB3`(a), and `NB11` (b).

3.1 Bubble size distribution

We track bubbles and evaluate the diameter of an equivalent circle $D_i(t) \equiv \sqrt{4A_i(t)/\pi}$ from their area, where the subscript i indicates the bubble index. In Fig. (3a-c), we plot the probability distribution function (pdf) of the bubble diameter $P(D)$ for different values of Ga and Bo. The competition between breakups and coalescence of bubbles due to the flow determines the pdf shape. For large Bo > 1 (small σ), the breakup of bubbles is more dominant than coalescence, and the pdf's peak is to the left of the initial bubble diameter d. On reducing the Bo (increasing σ), coalescence becomes more dominant than breakups, the pdf broadens, and a secondary peak starts to appear at $D > d$.

Consider a bubble whose diameter is the same as the average bubble diameter $\mathcal{D}$ in the suspension, where

$$\mathcal{D} = \int DP(D)dD. \tag{2}$$

The rise velocity of this bubble $U \sim \sqrt{\phi\delta\rho g\mathcal{D}/\rho_f}$ is determined by the balance of buoyancy with the drag [1]. Whether such a rising bubble breaks or not can be estimated by balancing the 2D bubble kinetic energy $\sim \rho_f U^2\mathcal{D}^2$ with the bubble surface energy $\sim \sigma\mathcal{D}$ [1] to get,

$$\mathcal{D} \sim \sqrt{\frac{\sigma}{\phi\delta\rho g}} \equiv \frac{d}{\sqrt{\phi \mathrm{Bo}}}. \tag{3}$$

In Fig. (3d) we plot the average bubble diameter $\mathcal{D}$ (2) for all the runs given in Table 1 and find it to be in good agreement with the theoretical prediction (3).

In the following, we first discuss the steady-state energy budget and derive the scale-by-scale energy budget equations in Sections 3.2 and 3.3. Using these, we then investigate the energy spectrum and dominant balances by varying Ga and At numbers.

3.2 Kinetic energy budget

Taking the dot product of Eq. (1b) with $\boldsymbol{u}$ and then performing spatial averaging, we obtain the following equa-

[1] Note that in 3D, the balance of the bubble kinetic energy $\sim \rho_f U^2\mathcal{D}^3$ with bubble surface energy $\sim \sigma\mathcal{D}^2$ also gives (3).

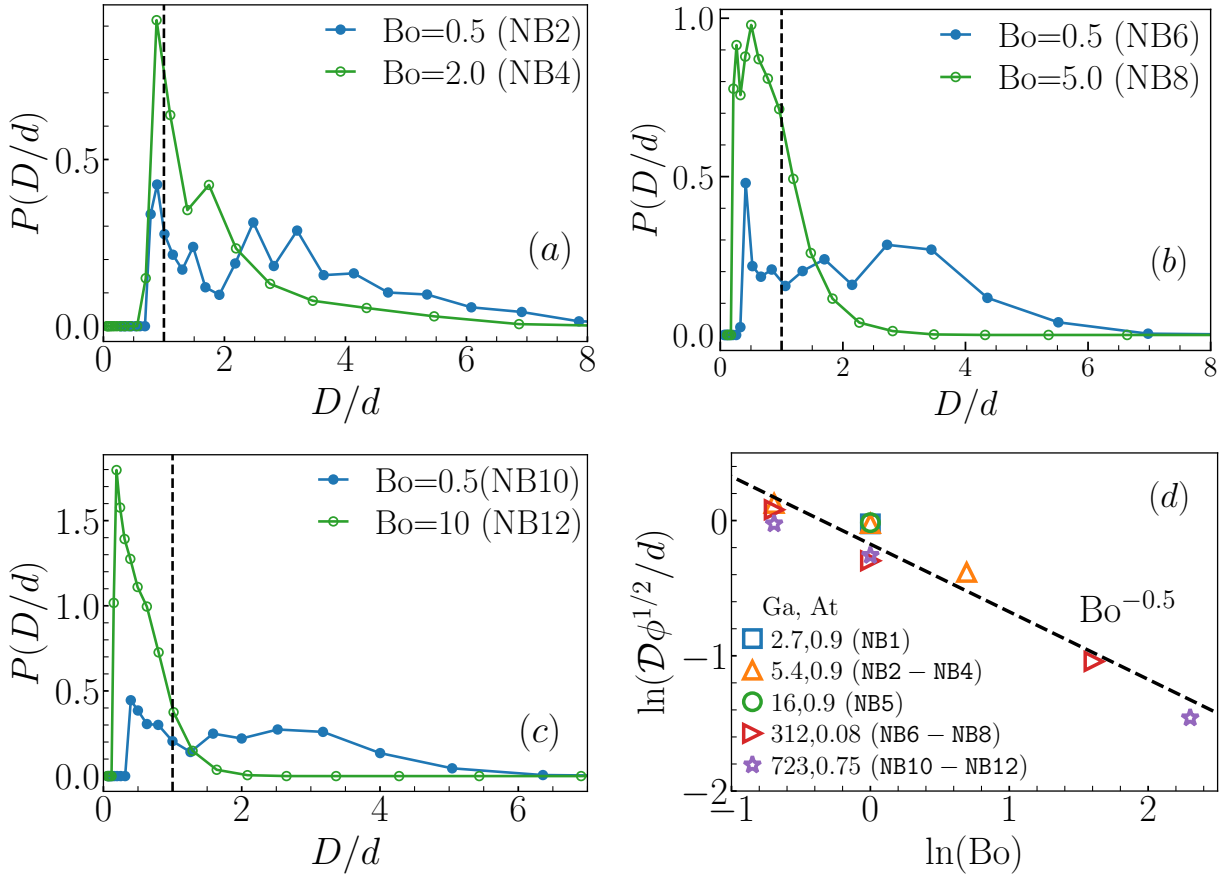

Fig. 3. (a-c) Pdf of the bubble diameter $P(D/d)$ versus D/d for different Bo and Ga [(a) Ga = 5.4, (b) Ga = 312, and (c) Ga = 723]. The vertical dashed line marks the initial bubble diameter. (d) Plot of the average bubble diameter $D\phi^{1/2}/d$ versus Bo for different combinations of Ga and At (runs `NB1-NB12`). The black line shows the theoretical prediction (3).

tion for the evolution of the total energy [11]:

$$\partial_t(\underbrace{\frac{1}{2}\overline{\rho \boldsymbol{u}^2}}_{E} + \underbrace{\overline{\sigma ds}}_{E_\sigma}) = -\underbrace{2\overline{\mu(c)\mathcal{S}:\mathcal{S}}}_{\epsilon_\mu} + \underbrace{\overline{[\rho_a - \rho(c)]u_y g}}_{\epsilon_{inj}}, \quad (4)$$

where $\overline{\boldsymbol{F^\sigma}\cdot\boldsymbol{u}} = \partial_t E_\sigma = \partial_t \int(\sigma ds)$ is the surface energy and ds is the surface element [42]. It is easy to verify from Table 1 that in the statistically steady state $\epsilon_{inj} \approx \epsilon_\mu$. It is important to note that the presence of spurious currents at bubble interface leads to additional numerical dissipation in VOF as well as front-tracking method [39, 43]. These effects are typically severe at large Ga and At [21]. Therefore, even for moderate Ga and At, we use high grid resolution and observe reasonable agreement between steady state values of ϵ_μ and ϵ_{inj} (see Table 1).

3.2.1 Energy dissipated by the wakes

As the bubbles rise within a swarm, the interaction of wakes leads to psuedo-turbulence. The energy dissipated by the wakes can be estimated as [15]

$$\epsilon_w \sim C_D \phi \rho_f (\delta\rho g \mathcal{D}/\rho_f)^{3/2}/\mathcal{D}, \quad (5)$$

where C_D is the drag coefficient. Assuming ϵ_w to be the dominant dissipation mechanism, we expect it to be comparable to both the viscous dissipation ϵ_ν and the energy injected by buoyancy ϵ_{inj}. Although it is difficult to estimate the bubble suspension's drag coefficient, we find $\epsilon_{inj} \approx \epsilon_w$ with $C_D = 1/2$ (see Fig. (4) and Table 1).

3.3 Energy spectrum and scale-by-scale energy budget

The energy spectrum E_k^{uu} and the co-spectrum $E_k^{\rho uu}$ are defined as follows:

$$E_k^{uu} \equiv \sum_{k-1/2<m<k+1/2} |\hat{\boldsymbol{u}}_m|^2,$$
$$E_k^{\rho uu} \equiv \sum_{k-1/2<m<k+1/2} \Re[(\hat{\rho\boldsymbol{u}})_{-m}\hat{\boldsymbol{u}}_m] \equiv d\mathscr{E}_k/dk.$$

We follow the procedure described in [11,31] and apply a low-pass filter to Eq. (1b) to obtain the following energy budget equation

$$\partial_t \mathscr{E}_k = -\Pi_k - \mathscr{P}_k + \mathscr{D}_k + \mathscr{F}_k^\sigma + \mathscr{F}_k^g, \quad (6)$$

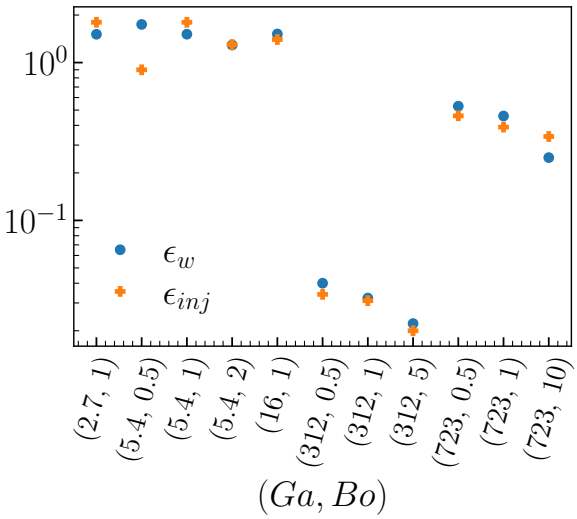

Fig. 4. Comparison of the energy injection rate ϵ_{inj} and the estimation of the dissipation rate due to the bubble wakes (5) [15] for different (Ga, Bo) [runs `NB1-NB12`].

with

$$\mathscr{E}_k = \frac{1}{2}\overline{\boldsymbol{u}_k^< \cdot (\rho\boldsymbol{u})_k^<},$$
$$\Pi_k = \frac{1}{2}\overline{(\rho\boldsymbol{u})_k^< \cdot (\boldsymbol{u}\cdot\nabla\boldsymbol{u})_k^<} + \overline{\boldsymbol{u}_k^< \cdot (\boldsymbol{u}\cdot\nabla\rho\boldsymbol{u})_k^<},$$
$$\mathscr{D}_k = \frac{1}{2}\overline{(\rho\boldsymbol{u})_k^< \cdot (\nabla\cdot[2\mu\mathcal{S}]/\rho)_k^<} + \overline{\boldsymbol{u}_k^< \cdot (\nabla\cdot[2\mu\mathcal{S}])_k^<},$$
$$\mathscr{F}_k^\gamma = \frac{1}{2}\overline{(\rho\boldsymbol{u})_k^< \cdot (\boldsymbol{F}^\gamma/\rho)_k^<} + \overline{\boldsymbol{u}_k^< \cdot (\boldsymbol{F}^\gamma)_k^<}, \text{ and}$$
$$\mathscr{P}_k = \frac{1}{2}\overline{(\rho\boldsymbol{u})_k^< \cdot (\nabla p/\rho)_k^<}.$$

Here, $\mathscr{E}_k$ is the cumulative energy up to wave-number k, Π_k is the energy flux through wave-number k, $\mathscr{D}_k$ is the cumulative energy dissipated, the contribution due to surface tension and buoyancy forces is $2\mathscr{F}_k^\gamma$ (γ represents either σ or g). In crucial departure from the uniform density flows, we find a non-zero cumulative pressure contribution $2\mathscr{P}_k$. The $<$ superscript above indicates low-pass filter upto wave-number k. Note that in the Boussinesq regime, the density field is uniform, i.e., $\rho = \rho_a$ and $\mathscr{P}_k = 0$ [11].

3.3.1 Low Ga, High At (`NB1` – `NB5`)

Initial studies in two-dimensions used the front-tracking algorithm and investigated buoyancy-driven bubbly flows at low Ga [19, 44, 45]. Below we compare results of our volume of fluid (VOF) simulations with identical parameters (see Table 1) as the 144-bubble front-tracking simulation in Ref. [19]. Note that in our simulations, in contrast to [19], the coalescence and breakup of the bubbles is allowed.

The plot of the kinetic energy spectrum E_k^{uu} and the co-spectrum $E_k^{\rho uu}$ (see Fig. (5a)) show the presence of a k^{-3} scaling for $k < k_d$. The energy spectrum obtained

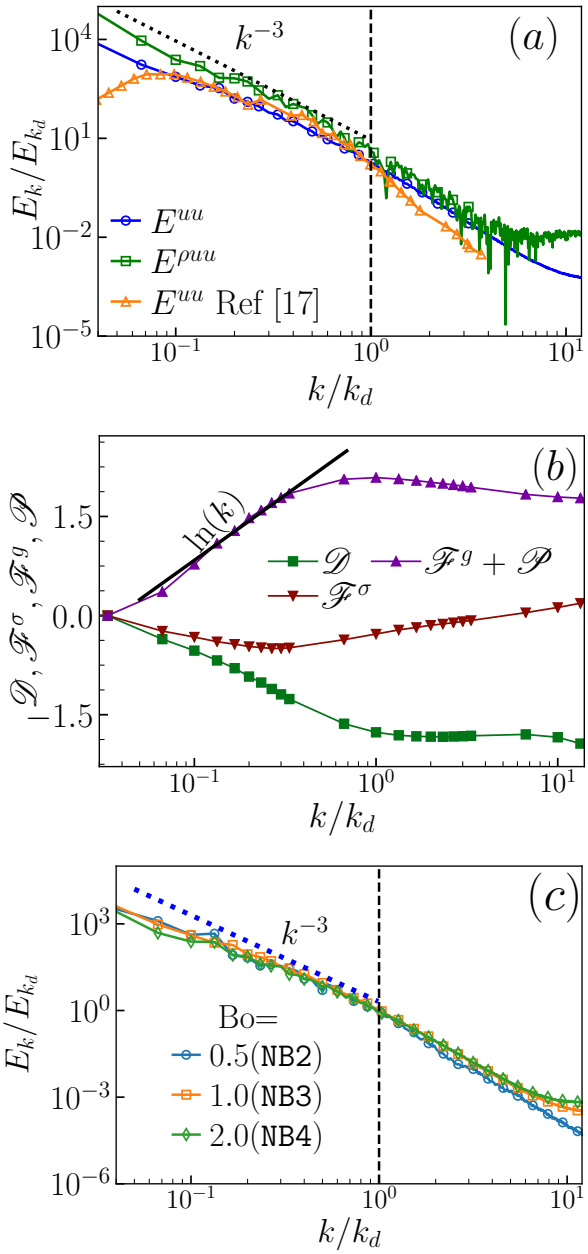

Fig. 5. (a) Log-log plot of spectrum and co-spectrum for `NB3`. Vertical dotted line represents $k = k_d$. (b) Semi-log plot of cumulative contribution due to viscosity $\mathscr{D}_k$, net energy injection $\mathscr{F}_k^g + \mathscr{P}_k$, and surface tension $\mathscr{F}_k^\sigma$. Least squares fit $(\mathscr{F}^g + \mathscr{P})_k = 0.85\ln(27.3k/k_d)$ [black line, $0.05 \le k/k_d \le 0.5$]. (c) Log-log plot of spectrum E_k^{uu} versus k/k_d for high At runs `NB2-NB4`.

from our DNS and [19] are in good agreement. The scale-by-scale energy budget analysis reveals that for $k < k_d$, dominant balance is between the net energy production and viscous dissipation. Assuming energy production to only depend on ϵ_{inj} and k [15], we expect the cumulative energy production $(\mathscr{F}^g + \mathscr{P})_k \sim \epsilon_{inj}\ln(k)$. Consistent with the predicted scaling, a least square fit in the range

$0.05 \leq k/k_d \leq 0.5$ gives $(\mathscr{F}^g + \mathscr{P})_k = 0.85\ln(27.3k/k_d)$ (see Fig. (5b)). The balance of net production $d(\mathscr{F}^g + \mathscr{P})_k/dk$ with viscous dissipation $\nu k^2 E_k^{uu}$ [Fig. (5b)] explains the observed scaling $E_k^{uu} \sim k^{-3}$ for $k \leq k_d$. The contribution due to surface tension $\mathscr{F}^\sigma$ is negligible in this regime. In Fig. (5c) we show that the scaling of the energy spectrum is insensitive to variations in Bo $= 0.5 - 2$.

3.3.2 High Ga, High At (NB10 – NB12)

On increasing the Ga number we find that the energy budget is dramatically altered. The spectrum E_k^{uu} and the co-spectrum $E_k^{\rho uu}$ (Fig. (6a)) show $k^{-5/3}$ scaling for $k < k_d$ and k^{-3} scaling for $k > k_d$. In Fig. (6b) we plot different contributions from the scale-by-scale energy budget equation. For $k < k_d$, the net energy injected $\mathscr{F}^g + P \sim \epsilon_{inj}\ln(k)$ is partly absorbed by surface tension and, similar to inverse energy cascade in fluid turbulence, we also find a negative energy flux Π_k for $k < k_d$. Not surprisingly, therefore, the energy spectrum $E_k^{uu} \sim k^{-5/3}$ [31] for $k < k_d$. For $k > k_d$, the energy absorbed by surface tension is redistributed to small-scales. Assuming the cumulative surface tension contribution to only depend on ϵ_w and k, we expect $\mathscr{F}_k^\sigma \sim \epsilon_w \ln(k)$ [Fig. (6b)]. A least square fit to $\mathscr{F}_k^\sigma$ confirms the logarithmic scaling. Finally, the balance viscous dissipation $\nu k^2 E_k^{uu}$ with the energy transfer because of the surface tension $d\mathscr{F}^\sigma/dk \sim k^{-1}$ explains the observed $E_k^{uu} \sim k^{-3}$ scaling. This balance for $k > k_d$ is similar to what has been observed in 3D pseudo-turbulence [11]. Finally, in Fig. (6c) we show that similar to the low Ga, the scaling of the energy spectrum is insensitive to the changes in the Bo.

3.3.3 High Ga, Low At (NB6 – NB8)

In the earlier section, we presented the results for pseudo-turbulence in the high Ga, high At number regime and showed that the statistical properties of PT are robust to changes in the Bond number. In this section, we show that the phenomenology of PT remains the same even for low At $= 0.08$ number. In Fig. (7a) we plot the spectrum for low At $= 0.08$ and show, similar to high At runs, $E_k^{uu} \sim k^{-5/3}$ for $k < k_d$ and $E_k^{uu} \sim k^{-3}$ for $k > k_d$ [2]. From our energy budget analysis we make the following observations (see Fig. (7b)): (i) For $k < k_d$ a non-zero energy flux Π_k; (ii) For $k > k_d$, $\Pi_k \approx 0$ and the energy injected by surface tension ($|\mathscr{F}_k^\sigma|$ increases)-because of bubble shape undulations- is balanced by viscous dissipation ($\mathscr{D}_k$ decreases). A non-zero Π_k indicates presence of an inverse energy cascade and hence, using Kolmogorov's phenomenology [31], $E_k^{uu} \sim k^{-5/3}$. On the other hand for $k > k_d$, the balance of energy redistributed by surface tension $\sim \epsilon_w/k$ with viscous dissipation gives $E_k^{uu} \sim k^{-3}$.

[2] We have also verified (not shown) that the scaling of the energy spectrum for At $= 0.08$ does not depend on the Bo.

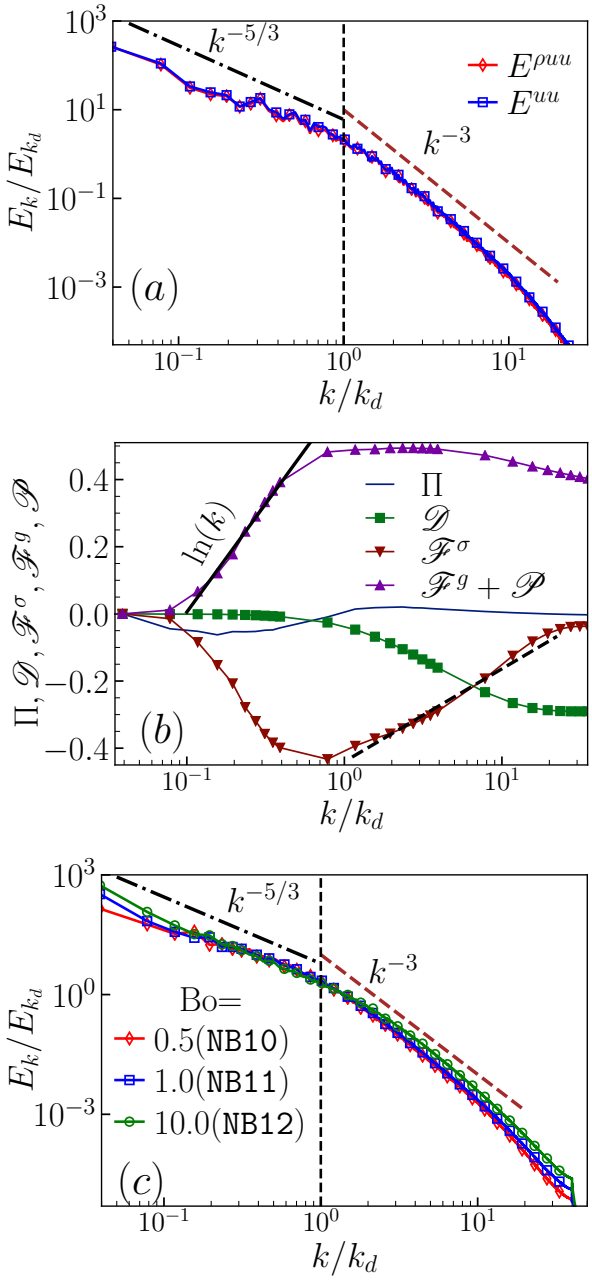

Fig. 6. (a) Log-log plot of the spectrum E_k^{uu} and the co-spectrum $E_k^{\rho uu}$ versus k/k_d for high Ga, high At run NB11. The dash-dot line indicates the $k^{-5/3}$ scaling whereas, the dashed line indicates k^{-3} scaling. The wave-number $k = k_d$ is shown by a vertical dotted line. (b) Cumulative contribution of viscous dissipation $\mathscr{D}_k$, energy flux Π_k, net cumulative energy injected $(\mathscr{F}^g + \mathscr{P})_k$, the surface tension contribution $\mathscr{F}_k^\sigma$. Least squares fits $(\mathscr{F}^g + \mathscr{P})_k = 0.28\ln(10.2k/k_d)$ (black dashed line, $0.12 \leq k/k_d \leq 0.6$), and $\mathscr{F}_k^\sigma = 0.12\ln(0.025k/k_d)$ (black dashed line, $1.1 \leq k/k_d \leq 15.0$). (c) Log-log plot of spectrum E_k^{uu} versus k/k_d for high At runs NB10 - NB12.

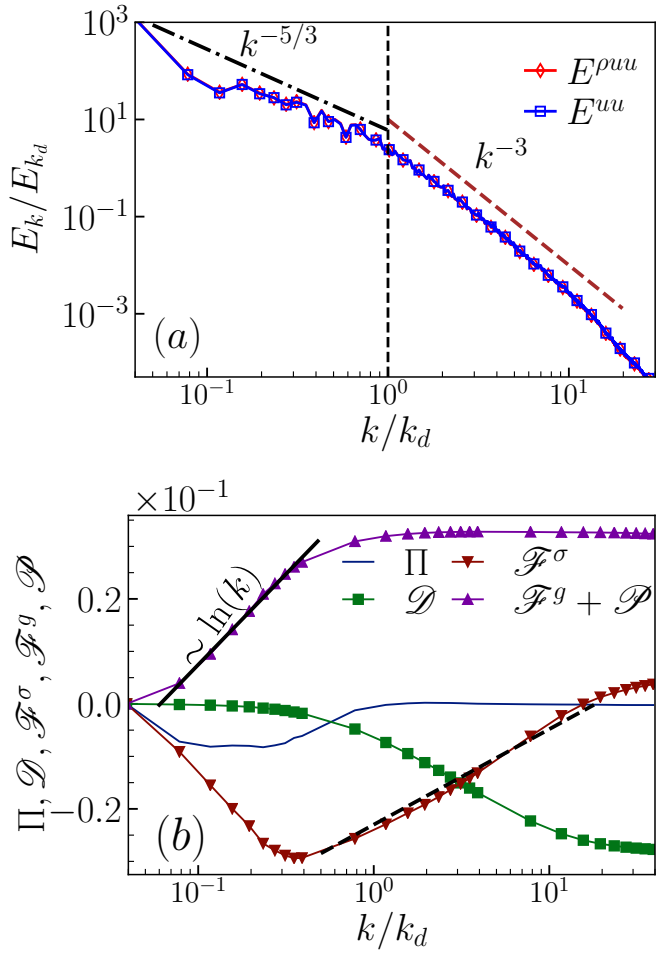

Fig. 7. (a) Log-log plot of the spectrum E_k^{uu} and the co-spectrum $E_k^{\rho uu}$ versus k/k_d for high Ga, low At run `NB7`. The dash-dot line indicates the $k^{-5/3}$ scaling whereas, the dashed line indicates k^{-3} scaling. The wave-number $k = k_d$ is shown by a vertical dotted line. (b) The energy flux Π_k, Cumulative contribution of viscous dissipation $\mathscr{D}_k$, net cumulative energy injected $\mathscr{F}_k^g + \mathscr{P}_k$, the surface tension contribution $\mathscr{F}_k^\sigma$. Least squares fits $(\mathscr{F}^g + \mathscr{P})_k = 0.015\ln(16.4k/k_d)$ (black line,$0.07 \le k/k_d \le 0.6$), and $\mathscr{F}_k^\sigma = 0.008\ln(0.06k/k_d)$ (black dashed line, $0.6 \le k/k_d \le 15.0$).

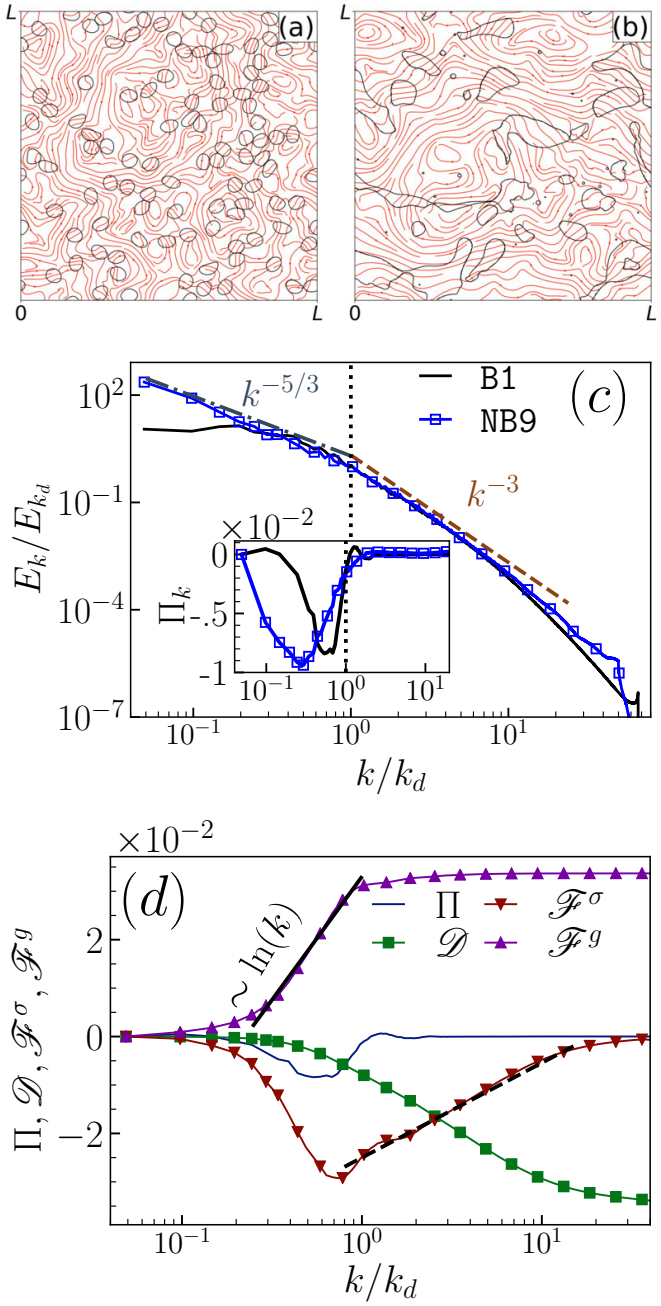

Fig. 8. (a,b) Representative steady-state snapshot of the velocity streamline with overlaid bubble positions for `B1` (front-tracking) and `NB9` (VOF) runs. (c) Log-log plot of energy spectra E_k^{uu} versus k/k_d for run `B1` and `NB9`. (Inset) Semilog plot showing negative energy flux Π_k versus k/k_d. Vertical dashed line corresponds to $k = k_d$. (d) Cumulative contribution of viscous dissipation $\mathscr{D}_k$, energy flux Π_k, energy injected because of buoyancy $\mathscr{F}_k^g$, and the surface tension contribution $\mathscr{F}_k^\sigma$ versus k/k_d for `B1`. Least squares fits $\mathscr{F}_k^g = 0.022\ln(4.3k/k_d)$(black line, $0.2 \le k/k_d \le 1.5$), and $\mathscr{F}_k^\sigma = 0.0085\ln(0.05k/k_d)$ (black dashed line, $1 \le k/k_d \le 15.0$. For $k < k_d$, $d\mathscr{F}_k^\sigma/dk$ balances $d\mathscr{F}_k^g/dk$ whereas, for $k > k_d$, $d\mathscr{F}_k^\sigma/dk$ is balanced by viscous dissipation $d\mathscr{D}_k/dk$.

3.3.4 Effect of merger and breakup (`B1`, `NB9`)

To further highlight the robustness of the energy spectrum, we conduct DNS using a front-tracking method [35] where breakup and coalescence of bubbles is not allowed. We refer the reader to [11] for details of the front-tracking scheme. We plot the snapshot of the bubble positions overlaid on the corresponding velocity streamlines for the front-tracking run `B1` and the bubble suspension from VOF run `NB9` in Fig. (8a,b). We find the bubbles are significantly deformed and their shape is nearly ellipsoidal. During the evolution, the average bubble diameter in `NB9` run remains close to the initial diameter. The energy spectrum obtained from our 2D runs (`B1` and `NB9`) are in excellent agreement, $E_k^{uu} \sim k^{-5/3}$ for $k < k_d$ and $E_k^{uu} \sim k^{-3}$ for

$k > k_d$ [Fig. (8c)]. Note that the region of negative energy flux (and $k^{-5/3}$ scaling) is broader for NB9 because coalescence and breakup leads to a bubble size distribution and an enhanced injection because of larger bubbles. Thus, coalescence of bubbles does not alter the scaling behaviour.

3.3.5 Pseudo-turbulence in 2D versus 3D

We now contrast the pseudo-turbulence spectral balances in 2D with our recent study in 3D [11]. In both cases, buoyancy injects energy at scales comparable to the bubble diameter. In 3D, the energy transfer due to the surface tension and forward kinetic energy flux balances viscous dissipation leading to the k^{-3} scaling for scales smaller than the bubble diameter. In contrast, in 2D, we show an inverse energy cascade from the bubble diameter scale to larger scales. Only the surface tension contribution transfers the energy to scales smaller than the bubble diameter. The viscous dissipation balances energy transfer by surface tension leading to the k^{-3} scaling.

4 Conclusion

To conclude, we have investigated the spectral properties of buoyancy driven bubbly flows. Using scale-by-scale energy budget we show that a non-zero negative energy flux in two-dimension that is indicative of an inverse cascade and leads to a $k^{-5/3}$ spectrum for scales larger than the bubble diameter. Although flow around an individual bubble strongly depends on the At [2,4,5,46], intriguingly, the scaling that we observe is not sensitive to the density contrast (At). Our scale-by-scale budget analysis reveals that in two-dimensional bubbly flows the k^{-3} scaling observed at large Ga is because of a balance between energy production due to surface tension and viscous dissipation.

R.R. conducted VOF simulations and V.P. conducted FT simulations. All authors analysed the results and reviewed the manuscript.

We thank D. Mitra and S. Banerjee for discussions, support from intramural funds at TIFR Hyderabad from the Department of Atomic Energy (DAE), India and DST (India) Project No. ECR/2018/001135.

References

1. R. Clift, J.R. Grace, M.E. Weber, *Bubbles, drops and particles* (Academic Press, New York, 1978)
2. D. Bhaga, M.E. Weber, J. Fluid Mech. **105**, 61 (1981)
3. E. Kelley, M. Wu, Phys. Rev. Lett. **79**, 1265 (1997)
4. X. Wang, B. Klaasen, J. Degrève, B. Blanpain, F. Verhaeghe, Phys. Fluids **26**, 123303 (2014)
5. M.K. Tripathi, K.C. Sahu, R. Govindarajan, Nat. Commun. **6**, 6268 (2015)
6. A. Filella, E. Patricia, V. Roig, J. Fluid Mech. **778**, 60 (2015)
7. R.F. Mudde, Annu. Rev. Fluid Mech. **37**, 393 (2005)
8. J.M. Mercado, D.G. Gómez, D.V. Gils, C. Sun, D. Lohse, J. Fluid Mech. **650**, 287–306 (2010)
9. F. Risso, Annu. Rev. Fluid Mech. **50**, 25 (2018)
10. V. Mathai, D. Lohse, C. Sun, Annu. Rev. Condens. Matter Phys. **11**, 529 (2020)
11. V. Pandey, R. Ramadugu, P. Perlekar, J. Fluid Mech. **884**, R6 (2020)
12. G. Riboux, F. Risso, D. Legendre, J. Fluid Mech. **643**, 509–539 (2010)
13. S. Mendez-Diaz, J.C. Serrano-Garcia, R. Zenit, J.A. Hernández-Cordero, Phys. Fluids **25**, 043303 (2013)
14. E. Bouche, V. Roig, F. Risso, A.M. Billet, J. Fluid Mech. **758**, 508–521 (2014)
15. M. Lance, J. Bataille, Journal of Fluid Mechanics **222**, 95–118 (1991)
16. E. Bouche, V. Roig, F. Risso, A.M. Billet, J. Fluid Mech. **704**, 211–231 (2012)
17. I. Roghair, J.M. Martinez, M.V.S. Annaland, H. Kuipers, C. Sun, D. Lohse, Int. J. Multiph. Flow **37**, 1093 (2011)
18. B. Bunner, G. Tryggvason, J. Fluid Mech. **466**, 53 (2002)
19. A. Esmaeeli, G. Tryggvason, J. Fluid Mech. **314**, 315–330 (1996)
20. R. Ramadugu, V. Pandey, P. Perlekar (2018), 1809.04759v1
21. A. Innocenti, A. Jaccod, S. Popinet, S. Chibbaro (2020), 2002.02209v1
22. R. Fjørtoft, Tellus **5**, 225 (1953)
23. R. Kraichnan, Phys. Fluids **10**, 1417 (1967)
24. C. Leith, Phys. Fluids **11**, 671 (1968)
25. G. Batchelor, Phys. Fluids **12**, II (1969)
26. G.L. Eyink, Physica D **91**, 97 (1996)
27. R. Pandit, P. Perlekar, S.S. Ray, Pramana **73**, 157 (2009)
28. R.H. Kraichnan, D. Montgomery, Rep. Prog. Phys. **43**, 3 (1980)
29. G. Boffetta, R.E. Ecke, Annu. Rev. Fluid Mech. **44**, 427 (2012)
30. R. Pandit, D. Banerjee, A. Bhatnagar, M. Brachet, A. Gupta, D. Mitra, N. Pal, P. Perlekar, S.S. Ray, V. Shukla et al., Phys. Fluids **29**, 111112 (2017)
31. U. Frisch, *Turbulence, A Legacy of A. N. Kolmogorov* (Cambridge University Press, 1997)
32. S. Pope, *Turbulent Flows* (Cambridge University Press, 2012)
33. K. Sreenivasan, R. Antonia, Annu. Rev. Fluid Mech. **29**, 435 (1997)
34. R. Benzi, L. Biferale, J. Stat. Phys. **161**, 1351 (2015)
35. G. Tryggvason, B. Bunner, A. Esmaeeli, D. Juric, N. Al-Rawahi, W. Tauber, J. Han, S. Nas, Y.J. Jan, J. Comput. Phys. **169**, 708 (2001)
36. https://cc.tifrh.res.in/index.php/kohinoor3/
37. J.U. Brackbill, D.B. Kothe, C. Zemach, J. Comput. Phys. **100**, 335 (1992)
38. S. Popinet, *Basilisk flow solver and* PDE *library*, http://basilisk.fr/ (2017)
39. S. Popinet, Annu. Rev. Fluid Mech. **50**, 1 (2018)
40. G. Tryggvason, R. Scardovelli, S. Zaleski, *Direct Numerical Simulations of Gas-Liquid Multiphase Flows* (Cambridge University Press, 2011)

41. A. Prosperetti, G. Tryggvason, *Computational Methods for Multiphase Flow* (Cambridge University Press, 2009), ISBN 9781139459907, https://books.google.co.in/books?id=KBuKZkEUWMIC
42. D.D. Joseph, *Stability of fluid motions II* (Springer Science & Business Media, 1976)
43. S. Popinet, S. Zaleski, Int. J. Numer. Methods Fluids **30**, 775 (1999)
44. A. Esmaeeli, G. Tryggvason, J. Fluid Mech. **377**, 313–345 (1998)
45. A. Esmaeeli, G. Tryggvason, J. Fluid Mech. **385**, 325–358 (1999)
46. S. Piedra, E. Ramos, J.R. Herrera, Phys. Rev. E **91**, 063013 (2015)